

PAPER • OPEN ACCESS

## Efficiency of dopant-induced ignition of helium nanodroplets

To cite this article: A Heidenreich *et al* 2016 *New J. Phys.* **18** 073046

View the [article online](#) for updates and enhancements.

### Related content

- [Dopant-induced ignition of helium nanodroplets—a mechanistic study](#)  
Andreas Heidenreich, Dominik Schomas and Marcel Mudrich
- [Evolution of dopant-induced helium nanodroplets](#)  
S R Krishnan, Ch Peltz, L Fechner *et al.*
- [Ion energetics in electron-rich nanodroplets](#)  
Andreas Heidenreich, Ivan Infante and Jesus M Ugalde

### Recent citations

- [Comparison of Electron and Ion Emission from Xenon Cluster-Induced Ignition of Helium Nanodroplets](#)  
Michael Kelbg *et al*
- [Cold physics and chemistry: Collisions, ionization and reactions inside helium nanodroplets close to zero K](#)  
A. Mauracher *et al*
- [Charging dynamics of dopants in helium nanodroplets](#)  
Andreas Heidenreich *et al*



## PAPER

## Efficiency of dopant-induced ignition of helium nanoplasmas

## OPEN ACCESS

RECEIVED  
24 March 2016REVISED  
16 June 2016ACCEPTED FOR PUBLICATION  
8 July 2016PUBLISHED  
26 July 2016

Original content from this work may be used under the terms of the [Creative Commons Attribution 3.0 licence](#).

Any further distribution of this work must maintain attribution to the author(s) and the title of the work, journal citation and DOI.

A Heidenreich<sup>1,2</sup>, B Grüner<sup>3</sup>, M Rometsch<sup>3</sup>, S R Krishnan<sup>4</sup>, F Stienkemeier<sup>3</sup> and M Mudrich<sup>3,5</sup><sup>1</sup> Kimika Fakultatea, Euskal Herriko Unibertsitatea (UPV/EHU) and Donostia International Physics Center (DIPC), P.K. 1072, E-20080 Donostia, Spain<sup>2</sup> IKERBASQUE, Basque Foundation for Science, E-48011 Bilbao, Spain<sup>3</sup> Physikalisches Institut, Universität Freiburg, D-79104 Freiburg, Germany<sup>4</sup> Department of Physics, Indian Institute of Technology—Madras, Chennai 600036, India<sup>5</sup> Author to whom any correspondence should be addressed.E-mail: [mudrich@physik.uni-freiburg.de](mailto:mudrich@physik.uni-freiburg.de)

Keywords: nanoplasma, helium nanodroplet, photoionization, molecular dynamics

## Abstract

Helium nanodroplets irradiated by intense near-infrared laser pulses ignite and form highly ionized nanoplasmas even at laser intensities where helium is not directly ionized by the optical field, provided the droplets contain a few dopant atoms. We present a combined theoretical and experimental study of the He nanoplasma ignition dynamics for various dopant species. We find that the efficiency of dopants to ignite a nanoplasma in helium droplets strongly varies and mostly depends on (i) the number of free electrons each dopant donates upon ionization, (ii) the pick-up process, and (iii) the hitherto unexplored effect of the dopant location in or on the droplet.

## 1. Introduction

Plasmas formed in nanoscale matter by the interaction with intense light pulses ranging from near-infrared (NIR) up to hard x-rays are a focus of current research. These studies are motivated by a large number of potential applications including the generation of energetic electrons and ions [1, 2] as well as intense XUV and attosecond pulses [3]. Besides, in single-shot x-ray imaging experiments of large molecules [4] and clusters [5], the creation of an expanding nanoplasma generally causes severe limitations to the achievable resolution of the initial structure. Controlling the nanoplasma dynamics for the purpose of exploiting its exceptional properties or for mitigating its detrimental effects requires in both cases a profound understanding of the dynamics of the ionization and time evolution of such nanoscale atomic and molecular systems in intense light fields.

In the NIR excitation regime, the remarkable properties of nanoplasmas have been rationalized by a resonant interaction between the external light field and the dipolar oscillations in the collective electron motion driven by this field [1, 2]. The resulting efficient light absorption induces avalanche-like charging and heating of the nanoplasma followed by hydrodynamic expansion and Coulomb explosion.

Atomic-scale design of nanoscopic targets provides an attractive route to controlling the ionization processes herein. Note that even random placement of water or carbon disulfide molecules as dopants into argon host clusters has resulted in significant enhancement of photon or electron emission [6, 7]. Novel resonant dynamics driven by ultrashort NIR laser pulses have been uncovered for superfluid helium (He) nanodroplets doped with a few xenon (Xe) atoms forming a dopant cluster in the droplet interior [8–17]. These reports have triggered a search for the optimal conditions for doping in such clusters.

Doped He nanodroplets are attractive candidates for probing the effects of dopants properties on the ionization dynamics. Due to its high ionization energy of 24.6 eV, the highest among all elements, He shows a high inertness to NIR radiation, requiring a threshold laser intensity of  $1.5 \times 10^{15} \text{ W cm}^{-2}$  for classical barrier suppression ionization (BSI). He droplets are therefore expected to show the largest effect upon doping with elements with lower ionization energies; for instance potassium (K), calcium (Ca) and Xe with their first ionization energies of 4.3, 6.1 and 12.1 eV, corresponding to a BSI threshold of  $1.4 \times 10^{12}$ ,  $5.5 \times 10^{12}$  and  $8.5 \times 10^{13} \text{ W cm}^{-2}$ , respectively.

Furthermore, He droplets offer the opportunity to vary the location of dopant atoms with high selectivity by appropriately choosing the atomic species, which is not possible for clusters of the heavier rare gases due to their solid structures [18, 19]. While most dopants such as rare gases submerge into the droplet interior, alkali metal atoms and small clusters reside in dimple-like states at the droplet surface [20–22]. Alkaline Earth metals represent an intermediate case in that they generally localize within the surface layer [19, 23].

In this paper we explore both in experiment and atomistic molecular dynamics (MD) simulations the capability of mono-elemental clusters of K, Ca and Xe dopants to trigger avalanche-like ionization of the He host droplets by NIR laser pulses far below the intensity regime at which pristine He droplets form nanoplasmas. The triggering of avalanche-like ionization we refer to as *ignition*. The goal of the simulations is to interpret the experimental observation that for different dopant species the ignition capability conspicuously varies as a function of the dopants physico-chemical properties. By choosing Xe, residing in the droplet interior, Ca in the surface layer, and K on the surface, we elucidate the effects of the dopant location, the dopant electronic properties and the dopant–He interatomic distance on He droplet ignition.

## 2. Experiment

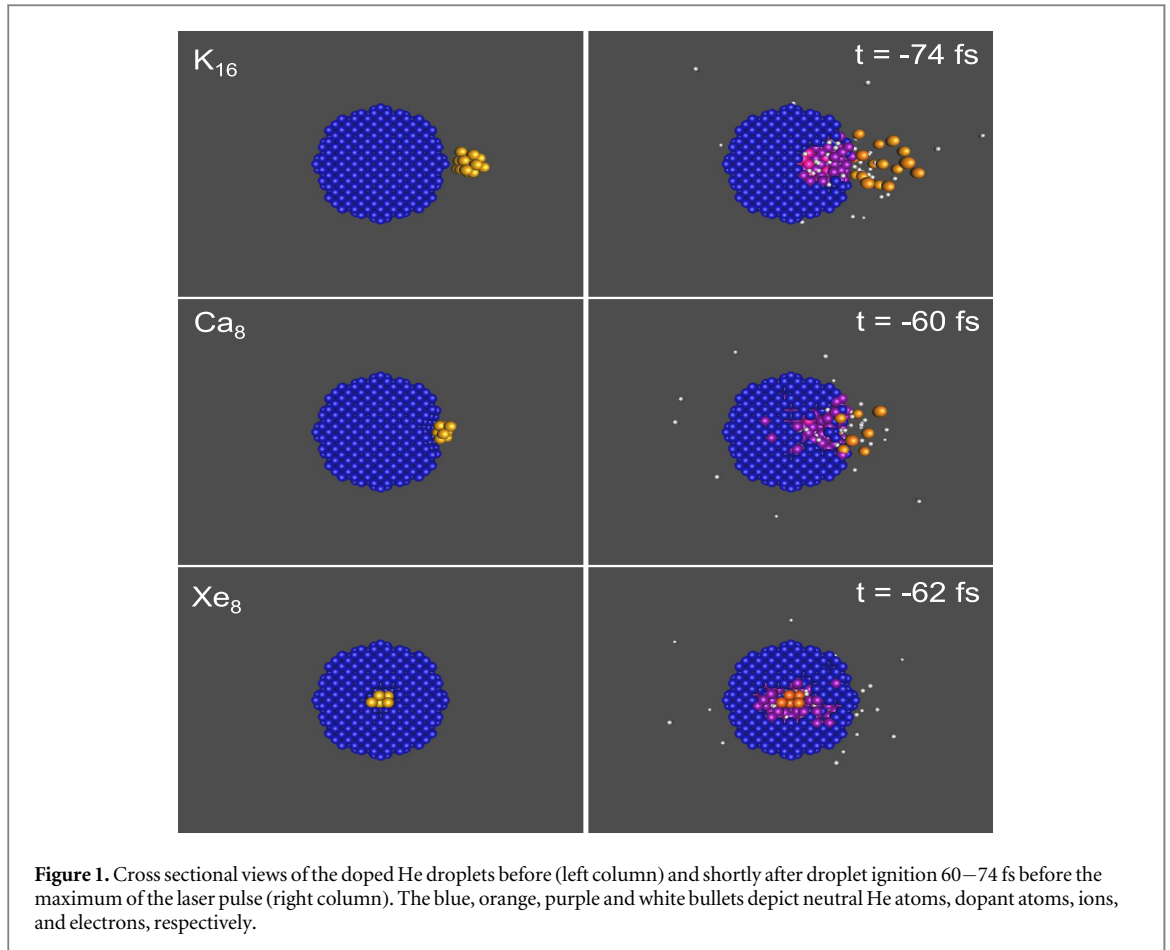
The experimental setup is composed of an amplified fs laser system for generating intense NIR laser pulses and a molecular beam apparatus for generating doped He nanodroplets. The latter has been described in detail elsewhere [15, 24]. In short, a beam of He nanodroplets is generated by continuously expanding pressurized He ( $p_0 = 50$  bar) of high purity (He 6.0) out of a cold nozzle ( $T_0 = 18$  K) with a diameter of  $5 \mu\text{m}$  into vacuum. At these expansion conditions, the mean droplet size is  $\langle N \rangle \approx 5000$  He atoms per droplet [18, 22]. The He droplets are doped with rare gas and metal atoms by passing through a scattering cell which contains atomic vapor with adjustable pressure. When increasing the doping pressure of either rare gas or metal vapor the He droplets pick up few atoms which aggregate to form clusters inside (rare gases) or at the droplet surface (alkali, alkaline Earth metals) [25]. At higher vapor pressures, the He droplets undergo massive scattering and shrinkage due to evaporation induced by the transfer of transverse momentum and the deposition of kinetic and binding energy (dopant–dopant and dopant–He). This leads to a general decrease in all droplet-correlated signals. The average number of dopants attached to the He droplets is inferred from the measured dopant partial pressure using detailed simulations of the pick-up process [26].

In the detector chamber, the doped He droplet beam crosses the focused laser beam at right angles in the center of a standard time-of-flight ion mass spectrometer. The laser pulses (central wave length  $\lambda = 800$  nm, pulse length  $t_{\text{FWHM}} = 220$  fs) are generated by chirped pulse amplification (Legend, Coherent Inc.) at a repetition rate of 5 kHz. The pulses are focused by a lens (focal length  $f = 75$  mm) placed inside the detector chamber to reach a maximum peak intensity  $I = 5 \times 10^{15} \text{ W cm}^{-2}$  in the focal volume.

## 3. Theory

The MD simulation method for the interaction of a cluster with the electric and magnetic field of a linearly polarized NIR Gaussian laser pulse was described previously [27–29]. All atoms and nanoplasma electrons are treated classically, starting with a cluster of neutral atoms. Electrons enter the MD simulation, when the criterion for tunnel ionization (TI), classical BSI or electron impact ionization (EII) is met. This is checked at each atom at every MD time step, using the local electric field at the atoms as the sum of the external laser electric field and the contributions from all other ions and electrons of the cluster. Instantaneous TI probabilities are calculated by the Ammosov–Delone–Krainov formula [30], EII cross sections by the Lotz formula [31] taking the ionization energy with respect to the atomic Coulomb barrier in the cluster [32]. The effect of chemical bonding on the valence shell ionization energies of K and Ca dopants is disregarded.

Coulomb potentials between ions, smoothed Coulomb potentials for ion–electron and electron–electron interactions are used. Interactions involving neutral atoms are disregarded except for a Pauli repulsive potential between electrons and neutral He atoms. The Pauli repulsive potential is expressed as a sum of pairwise fourth-order Gaussian functions centered at every neutral He atom,  $V(r_{ij}) = V_0 \exp(-r_{ij}^4/4\sigma^4)$ , with  $r_{ij}$  being the He–electron distance,  $V_0 = 1.1$  eV [33], and the exponent  $\sigma = 1.2 \text{ \AA}$  is chosen such that the effective range of  $V(r_{ij})$  is about half of the average He–He distance ( $3.6 \text{ \AA}$ ) in the neutral He droplet. The binding potentials of  $\text{He}_2^+$  and of other  $\text{He}_n^+$  complexes are not implemented, so that the MD simulations cannot account for the  $\text{He}_2^+$  formation explicitly; we can only estimate an upper bound of the  $\text{He}_2^+$  abundance from the remaining ground-state neutral He atoms and  $\text{He}^+$  ions at the end of each trajectory. Neutral He atoms and  $\text{He}^+$  ions which

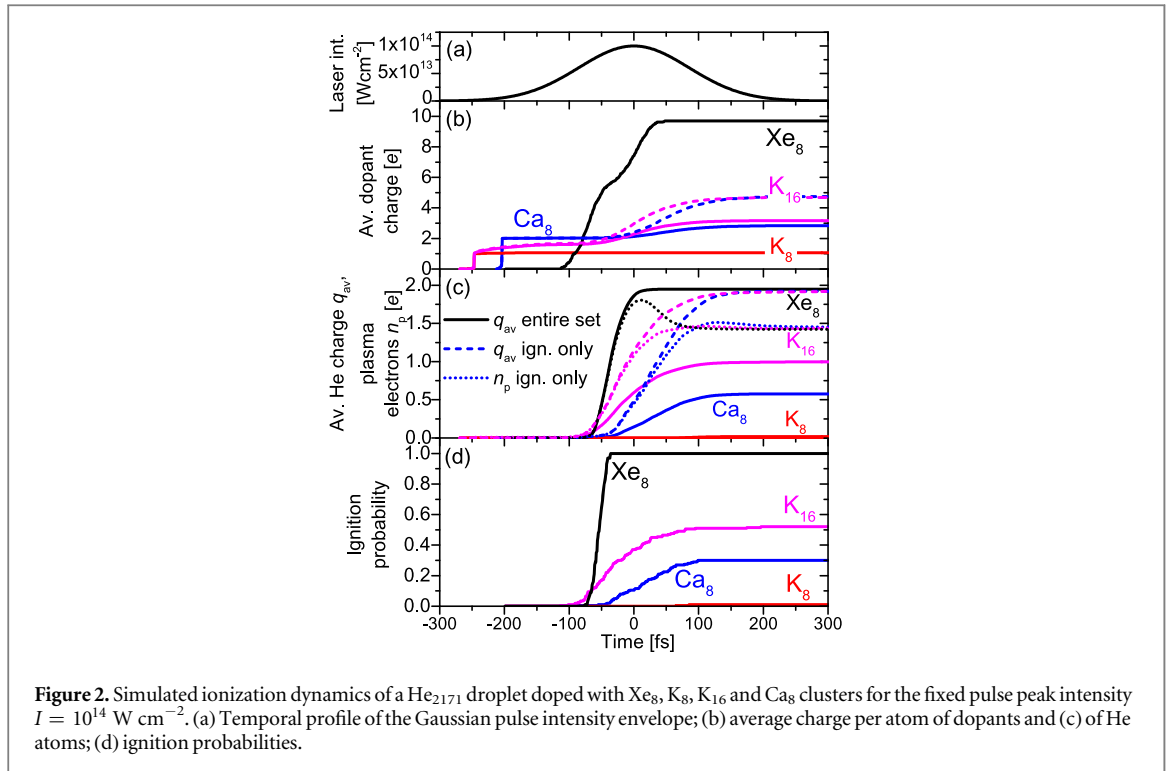


are formed by three-body electron–ion recombination are Rydberg state atoms and are therefore excluded from the estimate of the  $\text{He}_2^+$  production. Electron–ion pairs which are found within a cutoff distance of  $2 \text{ \AA}$  at the end of each trajectory (temporal length 0.7–1.8 ps) are taken to be recombined and the ion charge state abundances are corrected accordingly.

He ion and dopant ion signals are laser-intensity averaged over the three-dimensional focus volume [34] in the range  $8 \times 10^{12} - 5 \times 10^{15} \text{ W cm}^{-2}$ . Due to the high sensitivity of the droplet evolution to initial conditions, the results are averaged over sets of 5–100 trajectories per doped droplet and laser intensity. Moreover, surface-doped droplets (K and Ca) are averaged over their parallel and perpendicular orientations of the dopant–droplet axis with respect to the laser polarization axis unless mentioned explicitly. The temporal width of the Gaussian pulse intensity envelope is  $t_{\text{FWHM}} = 200 \text{ fs}$ , slightly lower than in the experiment (220 fs).

For the He droplets we assume a fcc structure with an interatomic distance of  $3.6 \text{ \AA}$  [35]. The dopant clusters are assembled according to the principle of densest packing of tetrahedra and to form, as far as possible, spherical shapes. We use the following interatomic distances: K–K  $4.56 \text{ \AA}$  (taken as the average interatomic distance in a  $\text{K}_{20}$  cluster) [36], Ca–Ca  $3.9 \text{ \AA}$  (average value for Ca clusters) [37], Xe–Xe  $4.33 \text{ \AA}$  (bulk), He–Xe  $4.15 \text{ \AA}$  [38], He–K  $7.13 \text{ \AA}$  [39], He–Ca  $5.9 \text{ \AA}$  (HeCa diatomic complex) [40]. In case of surface doping we assume a dimple depth of  $7 \text{ \AA}$  (inferred from density functional calculations of a single Ca atom on the surface of a He droplet) [23]. According to Ancilotto *et al* [21], a single K atom is located in a dimple of depth  $2.3 \text{ \AA}$ . Since such a shallow dimple cannot be implemented in a fcc lattice of discrete He atoms, we neglect the dimple for K dopants.

Figure 1 visualizes the starting configurations of our MD simulations (left column) as well as the ignition of the doped He droplets induced by the interaction with a laser pulse of peak intensity  $I = 10^{14} \text{ W cm}^{-2}$  (right column). The dopant–He complexes contain 2171 He atoms (cluster radius  $26.1 \text{ \AA}$ ) and the indicated number of dopant atoms. In the snapshots of the clusters at the indicated interaction times with respect to the maximum of the laser pulse (right column) the neutral He atoms are represented by blue spheres, dopant atoms are orange, ions are red and electrons are small white dots. These snapshots are chosen to illustrate the onset of nanoplasma formation shortly after dopant-induced ignition of the He droplet.



## 4. Results and discussion

### 4.1. Simulated ionization dynamics

To outline the microscopic processes evolving in the course of droplet ionization, figure 2 depicts MD simulation results for the time evolution of several characteristic quantities for selected dopant species. Shown are the intensity envelope of the laser pulse in panel (a) and, averaged over trajectory bundles, the charge per dopant atom (b) and per He atom (c), and the probability of igniting a He nanoplasma (d), for  $\text{He}_{2171}$  droplets doped with  $\text{K}_8$  and  $\text{K}_{16}$  (both on the surface),  $\text{Ca}_8$  (in a dimple on the surface) as well as  $\text{Xe}_8$  (in the center). The pulse peak intensity is  $I = 10^{14} \text{ W cm}^{-2}$ .

Ionization of the doped droplets starts with TI or BSI of the dopant (figure 2(b)) in the rising edge of the laser pulse. After a time delay which we call ‘incubation time’, ignition of the He droplet induced by EII occurs, manifested by the rise of the average He charge (figure 2(c)). The role of the dopant is to provide the seed electrons and to assist EII by lowering of the Coulomb barrier at He by the field of the dopant cations. EII is also by far the dominating ionization channel (typically  $> 95\%$ ) in the subsequent rapid charging up in the avalanche ionization [1, 2].

In case of K dopants, a single ionization per K atom occurs early in the pulse at  $t \approx -250 \text{ fs}$ . For  $\text{K}_{16}$ , the incubation time is 100–150 fs until the average He charge begins to rise. During the incubation time, EII of He competes with a partial drain (outer ionization [41]) of the seed electrons. This competition is not always in favor of EII. It turns out that, depending on slight variations of the trajectories’ initial conditions but for the same pulse parameters, either He ionization does not take place at all, ceases after a few He atoms, or ignition occurs. The sensitivity to the initial conditions is high for those dopant sizes and pulse parameters for which the occurrence of ignition is on the knife’s edge. Which factors contribute to the ignition and determine the incubation time, is subject of a detailed mechanistic study and will be published in a subsequent paper. We define an average He charge of 0.1 as an empirical criterion for the detection of ignition. The exact choice of the threshold value is uncritical in view of the rapid charging process in the He droplet. In those trajectories with ignition, the average charge per He atom jumps to almost 2 within 50–70 fs, and the trajectory set-averaged He charge jumps to 1.0 (figure 2(c)) with an ignition probability of 0.52. The ignition probabilities, derived as fractions of the number of trajectories with ignition, are shown in (figure 2(d)). The long-time ignition probabilities for  $\text{K}_8$ ,  $\text{Ca}_8$  and  $\text{Xe}_8$  doped droplets are 0.01, 0.30 and 1, respectively. With an ignition probability of 1, the  $\text{Xe}_8$  cluster has the highest ignition efficiency as compared to the K and Ca dopants of the same size. For  $\text{Xe}_8$ , the initial seed ionization begins much closer to the laser pulse peak ( $t \approx -100 \text{ fs}$ ) than for K and Ca dopants.

The  $\text{K}_8$  and  $\text{K}_{16}$  examples reveal a dopant cluster size effect: the ignition probability increases with the number of dopant atoms as a larger dopant cluster provides more seed electrons and a stronger electric field created by the sum of dopant ion charges, thereby assisting EII by reducing the Coulomb barrier at the adjacent

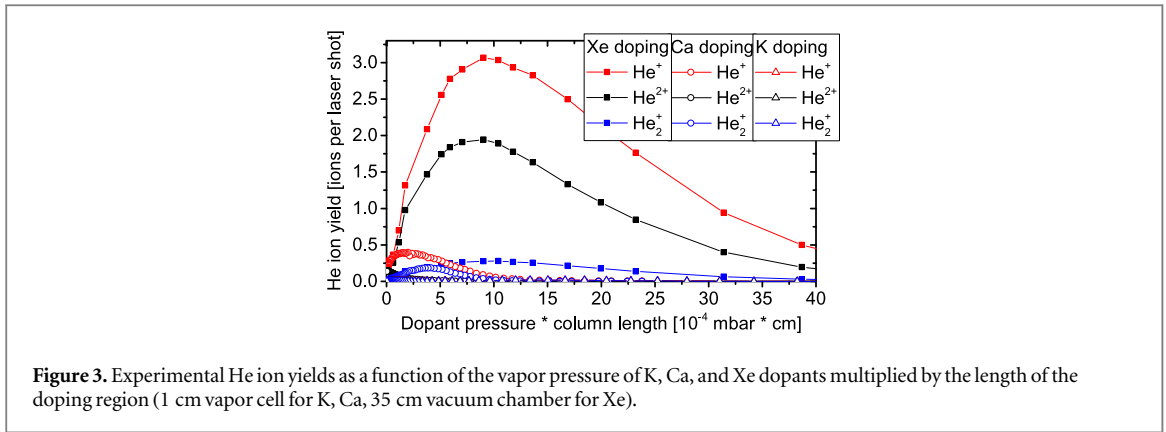


**Figure 3.** Experimental He ion yields as a function of the vapor pressure of K, Ca, and Xe dopants multiplied by the length of the doping region (1 cm vapor cell for K, Ca, 35 cm vacuum chamber for Xe).

He atoms. Moreover, the dopant cluster size effect is nonlinear: while for  $K_8$  the average charge per K atom remains 1 during the incubation time (figure 2(b)), for  $K_{16}$  it rises gradually, making via EII also up to two inner shell electrons available for seed ionizations.  $Ca_8$  contributes by its two valence electrons per atom.

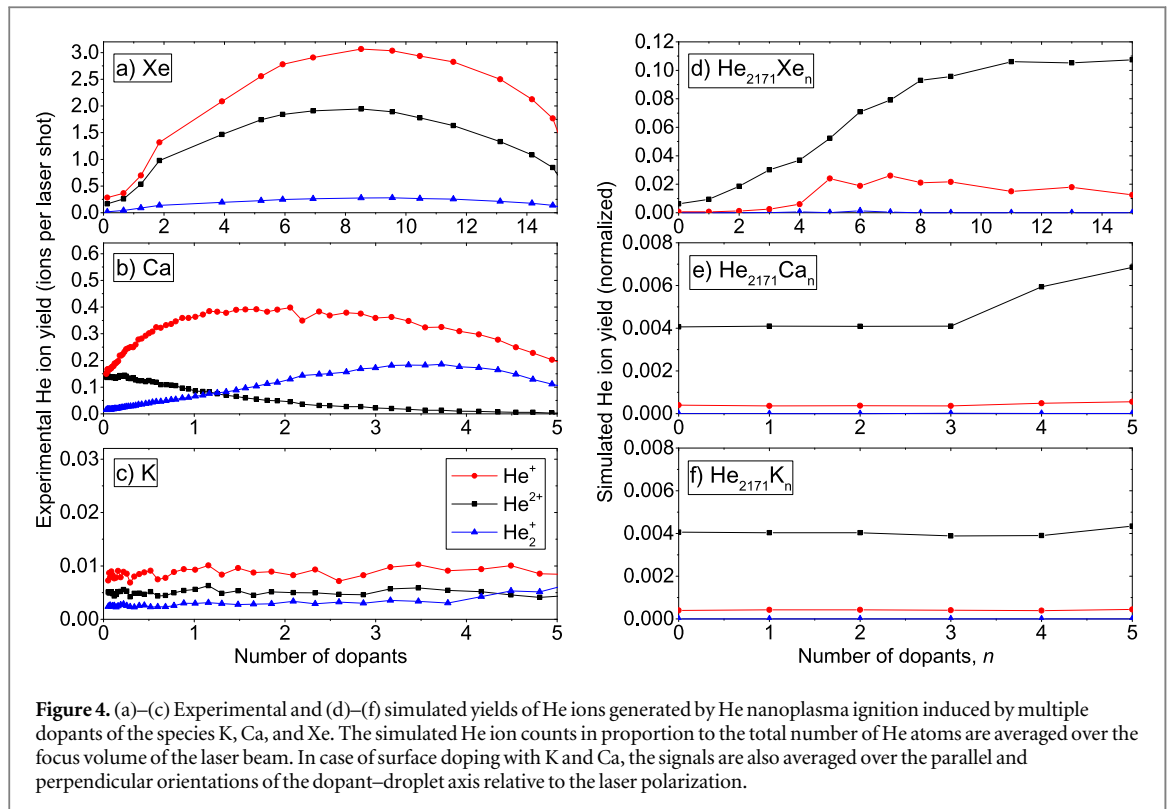
The outer ionization level in case of ignition can be derived from figure 2(c) as the difference of the average He charge  $q_{av}$  (solid line for  $Xe_8$  and dashed lines for the  $K_{16}$  and  $Ca_8$  doped droplets) and the nanoplasma electron population  $n_p$  per atom (dotted lines, obtained from the nanoplasma electrons within six droplet radii from the droplet center of mass). In all the three cases, the outer ionization amounts to about 0.5 elementary charges per atom. For the pulse parameters in figure 2 ( $I = 10^{14} \text{ W cm}^{-2}$ ,  $t_{FWHM} = 200 \text{ fs}$ ), ion–electron recombination and  $He_2^+$  formation does not occur; recombination becomes important for  $I \lesssim 2 \times 10^{13} \text{ W cm}^{-2}$  and  $He_2^+$  formation for  $I \lesssim 10^{13} \text{ W cm}^{-2}$ .

At first sight it is a surprising result that both the dopant and the He host atoms charge up to the highest charge states when doping with  $Xe_8$  ( $q_{av}(Xe) = 9.7$  and  $q_{av}(He) = 2$ ) in contrast to doping with the  $K_{16}$  cluster ( $q_{av}(K) = 3.2$  and  $q_{av}(He) = 1$ ), in spite of the higher first ionization energy of Xe (12.1 eV) than of K (4.3 eV). For the  $K_{16}$  and  $Ca_8$  dopants, the average dopant charge state is considerably enhanced in case of nanoplasma formation. This becomes apparent in figure 2(b) when comparing the dopant charges averaged only over trajectories with ignition (dashed lines) with the corresponding values averaged over the entire trajectory set (closed lines); in these examples the difference is about two elementary charges. We observed the enhanced dopant charging in all our MD simulations, whenever the ionization of the He host cluster was nearly complete (average He charge close to 2), which for the pulse parameters of this example ( $I = 10^{14} \text{ W cm}^{-2}$ ,  $t_{FWHM} = 200 \text{ fs}$ ) is almost always the case when ignition occurs. The enhanced dopant charging is comprehensible, since EII as the almost exclusive ionization channel critically depends on the laser-driven nanoplasma electron cloud. With an ignition probability of 1, the effect cannot be displayed for  $Xe_8$  in figure 2(b). An enhanced charging of Xe in doped He droplets in MD simulations has also been reported by Peltz *et al* [10].

#### 4.2. Comparison theory-experiment

The efficiency of igniting a He nanoplasma is manifested by the appearance of He ion signals. Figure 3 shows the experimental yield of  $He^+$ ,  $He^{2+}$ , and  $He_2^+$  ions recorded as a function of the vapor pressure of dopants. The latter is adjusted by controlling the temperature of the heated crucible in the case of K and Ca and by leaking Xe into the doping chamber using a dosing valve. The conspicuous result is that by far the highest He ion yields are obtained when doping with Xe, whereas doping with Ca and K provides lower He ion yields by about one and two orders of magnitude, respectively. When increasing the doping pressure starting from zero, the He ion yields first rise due to enhanced efficiency of the dopant-induced ignition process. The diminishing of ion yields for high doping pressures is a consequence of massive droplet beam depletion due to the release of binding energy when dopant atoms aggregate into clusters inside the droplets as well as scattering of the droplets away from the beam axis, as mentioned in section 2. Effectively both number density and size of the He droplets in the laser interaction region are thus reduced.

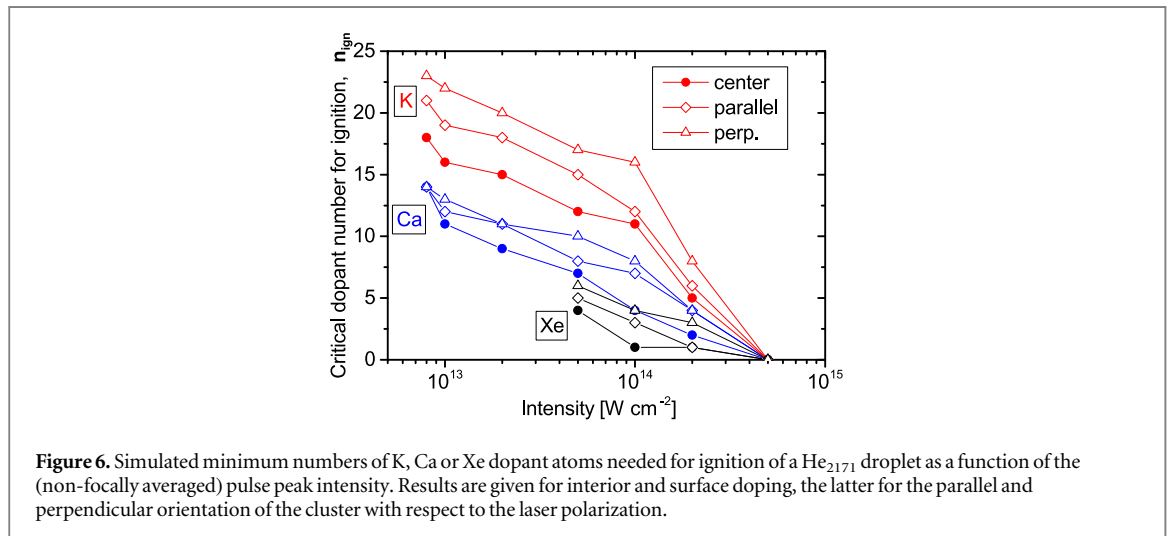
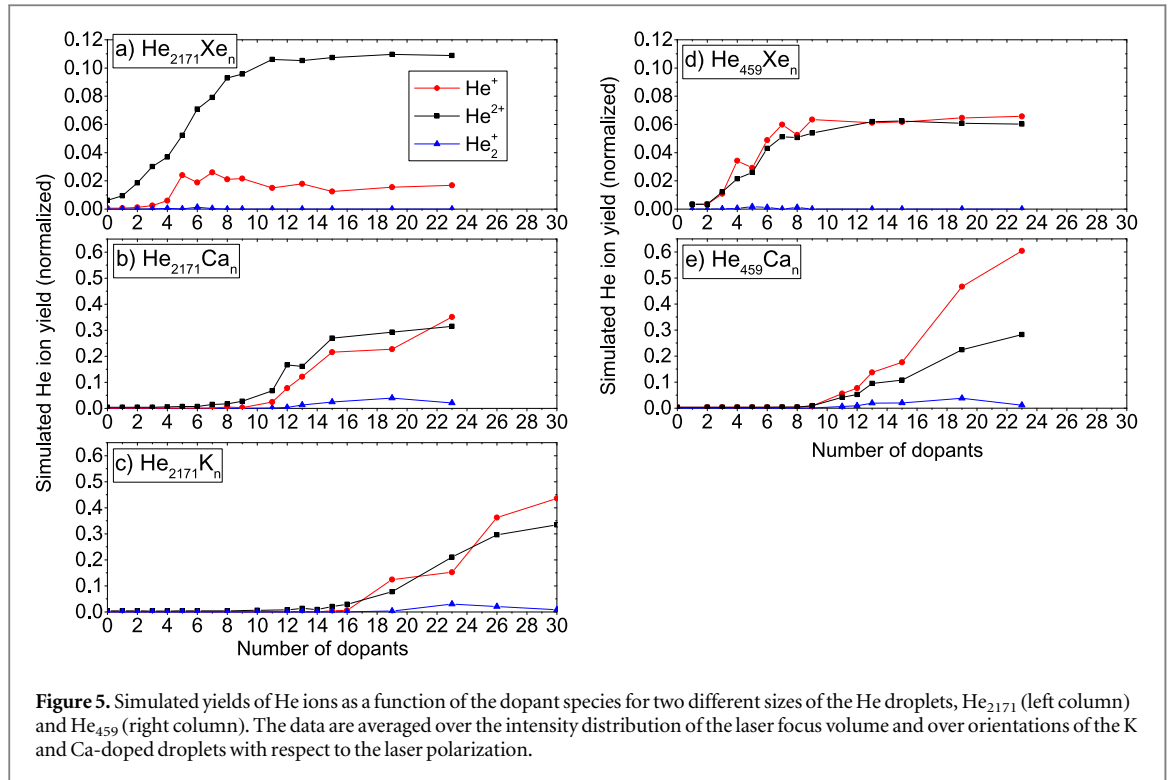
In an attempt to directly compare the experimental results with the MD simulation, the experimental data of figure 3 are represented on different x and y scales in figures 4(a)–(c). The rescaling of dopant pressure to the number of dopant atoms relies on the detailed simulation of the doping process [26]. The measured yields of  $He^+$  and  $He^{2+}$  ions as a function of the number of dopant atoms picked up on average by one droplet attains the highest values for Xe at about 13 dopant atoms. In contrast, the highest  $He^+$  signal observed for K-doping stays below that for Xe-doping by factor  $6 \times 10^{-3}$ . When doping with Ca atoms, the  $He^+$  ion yield comes close to the one obtained for Xe-doping at low doping numbers ( $n_{Xe} \leq 6$ ), but continuously falls off as the doping level is



increased. This diminishing of ion yields is primarily a consequence of massive droplet beam depletion by the large binding energy released when Ca clusters aggregate inside the droplets. Accordingly, the yield of  $\text{He}^{2+}$  ions sharply drops upon doping only a few ( $n_{\text{Ca}} = 2 - 3$ ) Ca atoms. The significant fraction of  $\text{He}_2^+$  observed for  $n_{\text{Ca}} = 3 - 6$  points at incomplete cluster ionization which is followed by dimer formation out of  $\text{He}^+$  surrounded by neutral He atoms.

A complete MD simulation of the ion signals requires (i) averaging over all intensities in the focal volume which contribute to the He ion signal, (ii) averaging over the size distribution of doped droplets, (iii) averaging over the dopant size distribution, and, for surface dopant states, (iv) averaging over the orientations of the dopant–droplet axis relative to the laser polarization. For the simulated He ion signals, figures 4(d)–(f), we have carried out only points (i) and (iv). Therefore, we cannot expect quantitative agreement between experiment and theory. As a consequence of the missing dopant size averaging, the abscissa of figures 4(d)–(f) represents a fixed number  $n$  of dopant atoms, whereas each value of the abscissa of the experimental signals, figures 4(a)–(c), is the average number of dopant atoms in a distribution.

The simulated results qualitatively reproduce the experimental He ion yields for the dopant sequence  $\text{Xe} > \text{Ca} > \text{K}$  in the regime of weak doping where the detrimental effects of droplet evaporation are nearly negligible. By far the largest He ion yields are obtained for Xe doping, in agreement with the experiment. However, the difference between He signal intensities for Ca and K doping seen in the experiment is not well captured by the simulation. For Ca and K doping, the small simulated signal intensities stem from intensities  $I \geq 5 \times 10^{14} \text{ W cm}^{-2}$  for which the He droplet ignites by itself because of TI of He. Only for  $n \geq 4$  for Ca and  $n \geq 5$  for K, a slight signal increase occurs when the dopants are able to induce ignition at the next lower intensity,  $I = 2 \times 10^{14} \text{ W cm}^{-2}$ , at which the focal volume is sampled. The much larger experimental signal intensity differences are likely caused by the admixture of signal intensities of larger dopants in the dopant size distribution, and is therefore not expected to be reproduced by the simulations. This tentative conclusion is supported by the observed increase of the simulated signals when increasing the dopant size. As the simulations show (figure 5), the intensity increase sets in at a smaller number of Ca than K atoms; signals of Ca-doped droplets are therefore expected to benefit more from contributions of droplets with larger dopant clusters. A further reason for the less pronounced gradation of ignition signals for K versus Ca doping might be the uncertainty of the dimple depth of Ca dopants. With an unknown dimple depth for  $\text{Ca}_n$  for  $n > 1$ , in a conservative approach we chose the dimple depth of  $7 \text{ \AA}$  of a single Ca atom [23] irrespective of the dopant cluster size. Comparative MD simulations for interior doping sites have shown that small  $\text{Ca}_n$  dopants ( $n \leq 6$ ) induce ignition at lower intensities than  $\text{K}_n$  clusters when brought into the droplet interior (see figure 6 and the



discussion in section 4.3). For example,  $\text{Ca}_2$  in an interior doping state induces ignition already at  $I = 2 \times 10^{14} \text{ W cm}^{-2}$ , unlike  $\text{K}_2$ .

Likewise, the decrease of the experimental signal for larger dopant clusters because of evaporation of He from the droplets cannot be accounted for in the MD simulation. The order of the  $\text{He}^+$  and  $\text{He}^{2+}$  signal intensities compared to the experimental signal is reversed which we partly attribute to the contribution of smaller droplets in the broad He droplet size distribution. Simulations for the smaller  $\text{He}_{459}$  doped droplets (droplet radius  $15.8 \text{ \AA}$ ) as a sample of the droplet size distribution subjected to evaporation indeed show that the He ion abundance considerably shifts towards singly charged  $\text{He}^+$ , as shown in figures 5(d) and (e). An additional reason might be the disregard of interactions between He as well as dopant cations with neutral He in the MD simulations. The presence of neutral He atoms in partially ionized droplets may cause a reduction of the high charge states of both He as well as dopant cations by electron transfer. Besides, due to the formation of  $\text{He}_n^+$  complexes vibrational energy is deposited in the droplets and might influence the dynamics of droplet ionization. In this context we note that our current simulations underestimate the  $\text{He}_2^+$  yield. The role of ion-neutral interactions and of the formation of  $\text{He}_n^+$  complexes are the subject of forthcoming simulations.

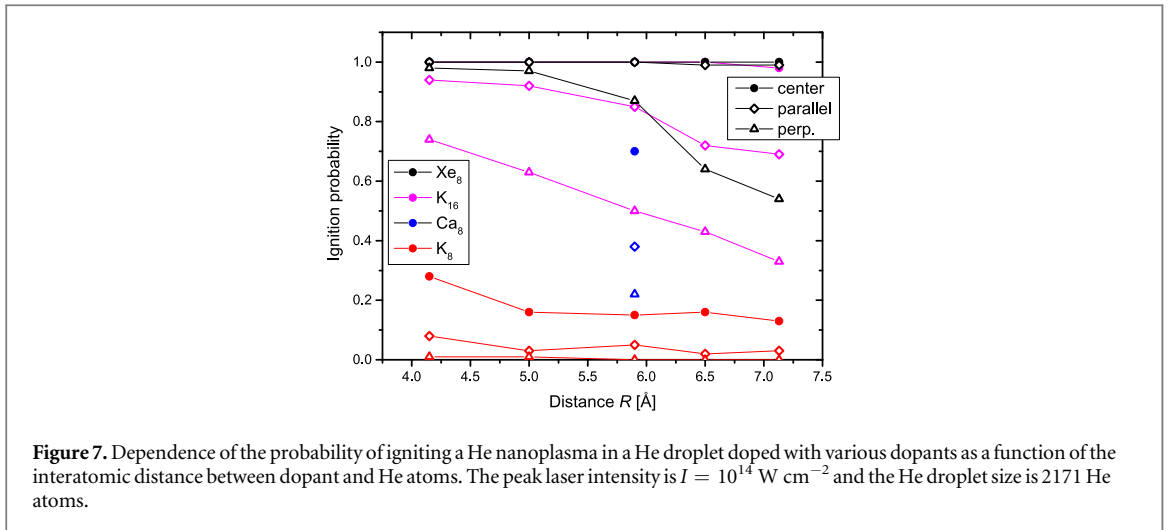


**Figure 7.** Dependence of the probability of igniting a He nanoplasma in a He droplet doped with various dopants as a function of the interatomic distance between dopant and He atoms. The peak laser intensity is  $I = 10^{14} \text{ W cm}^{-2}$  and the He droplet size is 2171 He atoms.

### 4.3. Optimizing dopant-induced ignition of He droplets

Since MD simulations are not limited by droplet beam depletion, we can study the hypothetical situation of attaching larger ( $> 10$ ) K and Ca dopant clusters to the He droplets. For these larger dopant clusters we find strongly enhanced He ion yields even for doping with Ca and K, see figure 5. The larger number of dopant atoms supply enough seed ionizations for He ignition at low laser intensities which make up the largest part of the laser focus volume. Note that, as a consequence of focal averaging, for doping with  $\gtrsim 11$  Ca or  $\gtrsim 19$  K atoms which make the low intensities in the periphery of the focus volume available for ignition, the yield of the He ions even exceeds the maximum yield reached for Xe doping. The largest considered dopants  $\text{K}_{30}$  and  $\text{Ca}_{23}$  induce partial ignition already below  $8 \times 10^{12} \text{ W cm}^{-2}$ . The contribution of these very low intensities is on the order of 10% and is neglected here. Since TI of Xe requires  $I \gtrsim 5 \times 10^{13} \text{ W cm}^{-2}$ , lower intensities remain inaccessible even for larger Xe dopants.

The systems considered in this work are dissimilar in various respects, given by the experimental boundary conditions: ionization energies and locations inside or at the droplet surface are different. In the experiment, droplet beam depletion upon cluster aggregation is a further dopant-specific limitation. What are the crucial factors for the observed conspicuous species-dependence of doped He nanodroplet ignition? In the following we systematically study the ignition efficiency of dopants in terms of their specific properties.

Figure 6 depicts the simulated minimum number  $n_{\text{ign}}$  of dopant atoms at which the ignition probability exceeds 10%. The variation of  $n_{\text{ign}}$  is shown as a function of the intensity  $I$ , for interior and surface dopant states. The latter ones are distinguished by parallel and perpendicular orientation of the dopant–droplet complex with respect to the linear laser polarization. The data clearly show three main trends in dopant-induced ignition:

(i) A lower intensity can be compensated to a large extent by larger dopant clusters. This is due to the larger number of seed electrons available for EII and by the higher sum of ion charges which assist EII by reducing the Coulomb barrier at He. In addition, for a given species the number of seed ionizations per dopant atom increases with the number of dopant atoms, as shown for the  $\text{K}_8$  and  $\text{K}_{16}$  dopants (see figure 2).

(ii) Dopants which are easily multiply ionized (Xe, Ca) are considerably favored, for the same reasons as in (i).

(iii) Dopants residing in the droplet interior ignite the neighboring He atoms more efficiently, as the cloud of seed electrons quivering in the driving laser field has better contact with the He host droplet. For all three dopants, a significantly larger number of dopants is needed for ignition of surface-bound dopant clusters at any laser intensity, where the parallel orientation is more favorable than the perpendicular one. Surface doping in parallel orientation typically requires 1–3 dopant atoms more to reach the same ignition efficiency as interior doping; the same gradation is found for surface doping between parallel and perpendicular orientation.

Another parameter which may severely impact the ignition efficiency of dopants attached to He droplets is the dopant–He interatomic distance as it affects the dopant–droplet contact strength as well. It is quite distinct for the three species under study and carries some uncertainty mainly due to unknown cluster size effects. Figure 7 displays the dependence of the He ignition probability on the dopant–He distance at the interface between the dopant cluster and the He host matrix for the dopant samples of figure 2.

Shown are the ignition probabilities in the interatomic distance range between the He–Xe (4.15 Å) and the He–K distance (7.13 Å) for interior as well as for surface doping in parallel and perpendicular orientation of the dopant–droplet axis relative to the laser polarization. While the general trend is, as expected, the decrease of the ignition probability with increasing He–dopant separation,  $\text{Xe}_8$  in its interior doping state is so efficient that its

ignition probability remains 1 in the entire considered distance range. In contrast,  $K_8$  does not reach the ignition probability of  $Xe_8$ , even when it is brought to the droplet interior at the shorter He–Xe distance, confirming that geometrical effects alone cannot account for the larger ignition capability of Xe. In our MD simulations we observed that at  $I = 10^{14} \text{ W cm}^{-2}$   $Xe_8$  is able to contribute up to three seed electrons per atom by TI, BSI and EII within the incubation time of a few fs, in contrast to only one seed electron per atom in the  $K_8$  case (figure 2(b)). This can be rationalized by the relatively low second and third ionization energies of Xe of 21.0 and 32.1 eV, respectively, compared to 31.6 and 45.7 eV for K, respectively. A further reason for the low ignition probability of  $K_8$  is its long incubation time. Delaying the seed ionization of  $K_8$  artificially until  $t = -100$  fs (the instant when TI sets in for Xe), the detrimental effect of outer ionization of the seed electrons is reduced and the ignition probability increases from 0.01 to 0.6.

## 5. Conclusions

Our investigations, theoretical and experimental, elucidate the efficiency of small mono-elemental (K, Ca, Xe) dopant clusters to ignite the nanoplasma formation of He nanodroplets exposed to intense NIR laser pulses. The conspicuous result is that Xe dopants induce by far higher yields and charge states of He ions as compared to Ca and K. Systematic MD simulations reveal that the dopants' efficiency in triggering ignition of He droplets at moderate laser intensities is predominantly determined by the ability of the dopant cluster to provide seed electrons. In particular, we find that the key to efficient dopant-induced ignition is the ease of multiple, not just single, ionization of dopant atoms (Xe). Surprisingly, low-lying first ionization energies of dopants (K, Ca) which maximize the useful interaction volume in the experiment are actually detrimental to ignition since long incubation times between ionization of dopants and He favor outer ionization of the seed electrons.

Additional important factors we identify are the doping site—inside or at the He droplet surface—and the He–dopant interatomic distance, both of which determine the contact strength of the laser-driven quivering electron cloud with the He droplet. As an experimental constraint, the release of dopants' heat of cluster formation induces partial evaporation of both dopants and He atoms off the droplets. Accordingly, among the considered dopant clusters, Xe has the highest ignition efficiency due to its unifying of the advantages of providing up to three seed ionizations per atom, occupying interior doping sites inside the He droplets, and releasing the lowest heat of dopant cluster formation. However, the first ionization energy imposes the limitation that seed ionization sets in only at  $I \gtrsim 5 \times 10^{13} \text{ W cm}^{-2}$ . In principle, if droplet evaporation by dopant cluster formation did not play any role, He nanoplasma ignition could be brought down to laser intensities  $I \lesssim 8 \times 10^{12} \text{ W cm}^{-2}$  by adding more atoms with low ionization energies (K, Ca). The possibility of optimizing the physico-chemical properties of dopant clusters by mixing various species inside the same He droplet, in particular to realize low threshold intensities with a few dopant atoms, will be studied in a forthcoming work.

## Acknowledgments

Stimulating discussions with Th Fennel, M Krishnamurthy and R Gopal are gratefully acknowledged. This work is supported by the Deutsche Forschungsgemeinschaft in the frame of the Priority Programme 1840 'Quantum Dynamics in Tailored Intense Fields'. The dissertation of B Grüner is supported by the Landesgraduiertenförderungsgesetz of Baden-Württemberg. We are grateful to Ivan Infante for prepublication information on inner-shell ionization energies of K and Ca. The authors thank for financial support from the Spanish Ministerio de Economía y Competitividad (ref. no. CTQ2015-67660-P), as well as for computational and manpower support provided by IZO-SGI SGIker of UPV/EHU and European funding (EDRF and ESF).

## References

- [1] Saalman U, Siedschlag C and Rost J M 2006 *J. Phys. B: At. Mol. Opt. Phys.* **39** R39
- [2] Fennel T, Meiwes-Broer K H, Tiggesbäumker J, Reinhard P G, Dinh P M and Surau E 2010 *Rev. Mod. Phys.* **82** 1793–842
- [3] Stebbings S L, Süßmann F, Yang Y Y, Scrinzi A, Durach M, Rusina A, Stockman M I and Kling M F 2011 *New J. Phys.* **13** 073010
- [4] Neutze R, Wouts R, van der Spoel D, Weckert E and Hajdu J 2000 *Nature* **406** 752–7
- [5] Gorkhover T et al 2012 *Phys. Rev. Lett.* **108** 245005
- [6] Jha J, Mathur D and Krishnamurthy M 2005 *J. Phys. B: At. Mol. Opt. Phys.* **38** L291
- [7] Jha J and Krishnamurthy M 2010 *Pramana* **75** 1181–9
- [8] Döppner T, Diederich T, Przystawik A, Truong N X, Fennel T, Tiggesbäumker J and Meiwes-Broer K H 2007 *Phys. Chem. Chem. Phys.* **9** 4639
- [9] Döppner T, Müller J, Przystawik A, Göde S, Tiggesbäumker J, Meiwes-Broer K, Varin C, Ramunno L, Brabec T and Fennel T 2010 *Phys. Rev. Lett.* **105** 53401
- [10] Peltz C and Fennel T 2011 *Eur. Phys. J. D* **63** 281–8

- [11] Göde S, Irsig R, Tiggesbäumker J and Meiwes-Broer K H 2013 *New J. Phys.* **15** 015026
- [12] Mikaberidze A, Saalman U and Rost J M 2008 *Phys. Rev. A* **77** 041201
- [13] Mikaberidze A, Saalman U and Rost J M 2009 *Phys. Rev. Lett.* **102** 128102
- [14] Krishnan S et al 2011 *Phys. Rev. Lett.* **107** 173402
- [15] Krishnan S R et al 2012 *New J. Phys.* **14** 075016
- [16] Krishnan S R, Gopal R, Rajeev R, Jha J, Sharma V, Mudrich M, Moshhammer R and Krishnamurthy M 2014 *Phys. Chem. Chem. Phys.* **16** 8721–30
- [17] Mudrich M and Stienkemeier F 2014 *Int. Rev. Phys. Chem.* **33** 301–39
- [18] Toennies J P and Vilesov A F 2004 *Angew. Chem., Int. Ed.* **43** 2622
- [19] Barranco M, Guardiola R, Hernández S, Mayol R, Navarro J and Pi M 2006 *J. Low Temp. Phys.* **142** 1
- [20] Stienkemeier F, Higgins J, Ernst W E and Scoles G 1995 *Phys. Rev. Lett.* **74** 3592–5
- [21] Ancilotto F, Cheng E, Cole M W and Toigo F 1995 *Z. Phys. B* **98** 323–9
- [22] Stienkemeier F and Lehmann K 2006 *J. Phys. B: At. Mol. Opt. Phys.* **39** R127
- [23] Hernando A, Mayol R, Pi M, Barranco M, Ancilotto F, Bünermann O and Stienkemeier F 2007 *J. Phys. Chem. A* **111** 7303–8
- [24] Mudrich M, Heister P, Hippler T, Giese C, Dulieu O and Stienkemeier F 2009 *Phys. Rev. A* **80** 042512
- [25] Lewerenz M, Schilling B and Toennies J P 1995 *J. Chem. Phys.* **102** 8191–207
- [26] Bünermann O and Stienkemeier F 2011 *Eur. Phys. J. D* **61** 645
- [27] Heidenreich A, Last I and Jortner J 2007 *J. Chem. Phys.* **127** 074305
- [28] Heidenreich A, Last I and Jortner J 2007 *Isr. J. Chem.* **47** 89–98
- [29] Heidenreich A, Infante I and Ugalde J M 2012 *New J. Phys.* **14** 075017
- [30] Ammosov A, Delone N and Krainov V 1986 *Sov. Phys.—JETP* **64** 1191
- [31] Lotz W 1967 *Z. Phys.* **206** 205
- [32] Fennel T, Rammunno L and Brabec T 2007 *Phys. Rev. Lett.* **99** 233401
- [33] Buchenau H, Toennies J P and Northby J A 1991 *J. Chem. Phys.* **95** 8134–48
- [34] Heidenreich A and Jortner J 2011 *J. Chem. Phys.* **134** 074315
- [35] Peterka D S, Kim J H, Wang C C, Poisson L and Neumark D M 2007 *J. Phys. Chem. A* **111** 7449
- [36] Banerjee A, Ghanty T K and Chakrabarti A 2008 *J. Phys. Chem. A* **112** 12303
- [37] Mirick J W, Chien C H and Blaisten-Barojas E 2001 *Phys. Rev. A* **63** 023202
- [38] Chen C H, Siska P E and Lee Y T 1973 *J. Chem. Phys.* **59** 601–10
- [39] Hauser A W, Gruber T, Filatov M and Ernst W E 2013 *Chem. Phys. Chem.* **14** 716–22
- [40] Hinde R J 2003 *J. Phys. B: At. Mol. Opt. Phys.* **36** 3119
- [41] Last I and Jortner J 1999 *Phys. Rev. A* **60** 2215